Analysis of temporomandibular joint dysfunction in paediatric patients with unilateral crossbite using automatically generated finite element models

Javier Ortún-Terrazas, José Cegoñino, Edson Illipronti-Filho & Amaya Pérez del Palomar

Taylor & Francis
Taylor & Francis Group

Analysis of temporomandibular joint dysfunction in paediatric patients with unilateral crossbite using automatically generated finite element models

Javier Ortún-Terrazas[a], José Cegoñino[a], Edson Illipronti-Filho[b] and Amaya Pérez del Palomar[a]

[a]Department of Mechanical Engineering, University of Zaragoza, Zaragoza, Spain; [b]Department of Stomatology, University of São Paulo, São Paulo, Brazil

ABSTRACT

The evaluation of temporomandibular joint (TMJ) dysfunction using finite element models is a time consuming process that requires extensive technical knowledge. We combined a statistical active appearance model with automated modelling algorithms to biomechanically study the relationship between TMJ malformations and dysfunction in radiographs from 20 paediatric patients with unilateral crossbite. A fitting algorithm (fitting error $< 4\%$) recognised the TMJ shape and adjusted the dimensions of each patient-specific 2D FE model, which was then used to compute 2 different joint movements. Significant functional differences were observed between the crossbite and non-cross bite sides, and the shape-function relation was verified.

Introduction

The temporomandibular joint (TMJ) is a complex mandibular articulator composed primarily of the TMJ disc, hyaline cartilages, and the disc attachments. The TMJ mainly develops during paediatric growth in response to the mechanical stimuli produced during chewing by the elevator (masseter, temporalis, medial pterygoid, and superior portion of the lateral pterygoid) and depressor (digastric, geniohyoid, mylohyoid, and the inferior portion of the lateral pterygoid) muscles (Bakke 2006; Chan et al. 2008). Healthy bilateral chewing occurs in an alternating manner: while one condyle compresses the TMJ disc with the mandibular fossa (working movement), the other moves the articular eminence forward (balancing movement) (Palla et al. 2003). While well-balanced chewing ensures proper development of both TMJs, unilateral crossbite (UXB) may result in morphological deformities in the TMJs.

Although the relationship between malformations and dysfunction has not been theoretically explained yet, some rehabilitation approaches (Prakash and Durgesh 2011; Planas 2013; Tsanidis et al. 2016) have empirically identified the morphological changes that take place. All of them agree that these pathological changes are exacerbated during growth, leading to severe temporomandibular joint disorders (TMD) in adulthood.

Early diagnosis could, therefore, help to correct malformations during childhood and avoid surgical procedures later in life (Dimitroulis 2018). For adults, 3D cephalometric images, such as computed tomography (CT) or cone-beam computed tomography (CBCT), are widely used to create 3D finite element (FE) models of the TMJs and evaluate its mechanical imbalance. Unfortunately, during childhood, these 3D approaches are not recommended due to the high doses of radiation involved in CT and CBCT scans (Planas 2013; Thiesen et al. 2015). Besides, the use of 3D FE models from CT or CBCT images is limited during childhood due to the low grey gradient between unmineralized structures at these ages. This fact makes difficult the segmentation procedure, requiring intensive manual work (Ortún-Terrazas et al. 2020). As an alternative, panoramic radiographs or 2D-cephalograms in frontal, lateral, and submento-vertex views are currently used to evaluate the morphological differences between both joints during childhood. Nevertheless, 2D imaging methods provide limited data to the clinician and not allow the

mechanical evaluation of the TMJs' imbalance. Fortunately, new approaches have enabled partial automation of FE model generation through the use of statistical deformable models. Among other applications, statistical deformable models have allowed automation of medical image segmentation (Shan et al. 2006), shape recognition (Dornaika and Ahlberg 2006), and disease diagnosis (Bredbenner et al. 2010).

The active appearance model (AAM) is a statistical deformable model that is often used for shape recognition in planar radiographs because it separately considers variations in shape and appearance (Cootes et al. 1995). The shape recognition process requires a minimisation function, which minimises differences between an input image and the texture instance of a previously developed AAM. The inverse compositional (IC) algorithm is one method commonly used for this fitting process, (Baker and Matthews 2004). However, IC algorithms are highly sensitive to the initialisation step and to texture variations in input and target images. Therefore, it is advisable to use highly-descriptive, dense appearance features to increase data dimensionality and thereby improve recognition accuracy (Antonakos et al. 2015). The most widely used appearance features include histograms of oriented gradients (HOG) (Dalal and Triggs 2005), image gradient orientation kernel (IGO) (Tzimiropoulos et al. 2012), scale-invariant feature transform (SIFT) (Ojala et al. 2001), local binary patterns (Lowe 1999), edge structures (Cootes and Taylor 2001), and Gabor filters (Lee 1996).

The goal of this study was therefore to create a tool for automated generation of planar FE models of the TMJ based on panoramic radiographs to study the relationship between TMJ malformations and UXB in a large, patient-specific dataset.

To this end, we propose a methodology that combines AAMs and automated modelling techniques and that it can be divided in 3 main steps. First, an image recognition algorithm recognises the TMJ shape in an area of a panoramic radiograph using an alternative of the IC algorithm that varies the shape and appearance parameters of a previously trained AAM. Next, the landmarks of the recognised shape are used to construct a parametric FE model using a modelling script. The 2 main TMJ movements (working and balancing) are then automatically computed for each patient-specific 2D model. Additionally, four 3D models of the stomatognathic system of 4 subjects were developed from the CBCT images and the lateral chewing was simulated. Finally, the differences between 2D and 3D modelling are evaluated by comparing the mechanical results produced by the 2D and 3D models of the same patient.

Materials and methods

This section describes the 3 main steps (Figure 1) involved in automating model generation. We first provide a summary of the data acquisition procedure, followed by a description of the AAM and the IC recognition algorithms. An animated presentation of the AAM development and recognition process is shown in the video of the supplementary material. Finally, we describe the 2D FE model in both loading scenarios, the statistical analyses performed, and the development of four 3D FE models in order to validate the 2D results.

Data acquisition

The input data consisted of 20 panoramic radiographs obtained from CBCT images of paediatric subjects (9 males and 11 females; mean age 7.9 and 8.2 years, respectively) in mixed dentition phase with UXB. The images were obtained in maximum intercuspation through the same CBCT scanning system (i-CAT^{TM}; Imaging Sciences International, Hatfield, PA, USA), with a field of view (FOV) of 13 cm $\times$ 17 cm, a pulse exposure acquisition time of 5–26 s, 14-bit greyscale, and 16,384 shades of grey. The focal point was at 0.5 m with a 0.3-mm voxel. The study was approved by the Research Ethics Committee of the School of Dentistry, University of São Paulo (200/06 and 16/2008). More details can be found in Illipronti-Filho et al. (2015). Data were converted to DICOM format and the panoramic views were extracted by iCAT Vision software (Imaging Sciences International Inc., Hatfield, PA, USA). The radiographs were divided into 2 groups (15 and 5 images) for the AAM training and the IC testing processes. From each radiograph, 2 patch images of both TMJs were extracted and the cross bite side TMJ was identified for subsequent analysis of the results.

Active appearance model with HOG feature

The AAM was defined in an open source code (Alabort-i-Medina et al. 2014) written in Python (Python 2.7.3, Python Software Foundation) and was run in a Windows-based personal computer with an Intel Core i7-6700 3.40 GHz processor and 32 Gb of RAM. The description of the AAM was computed in 86.07 s and the AAM was composed of 3 different
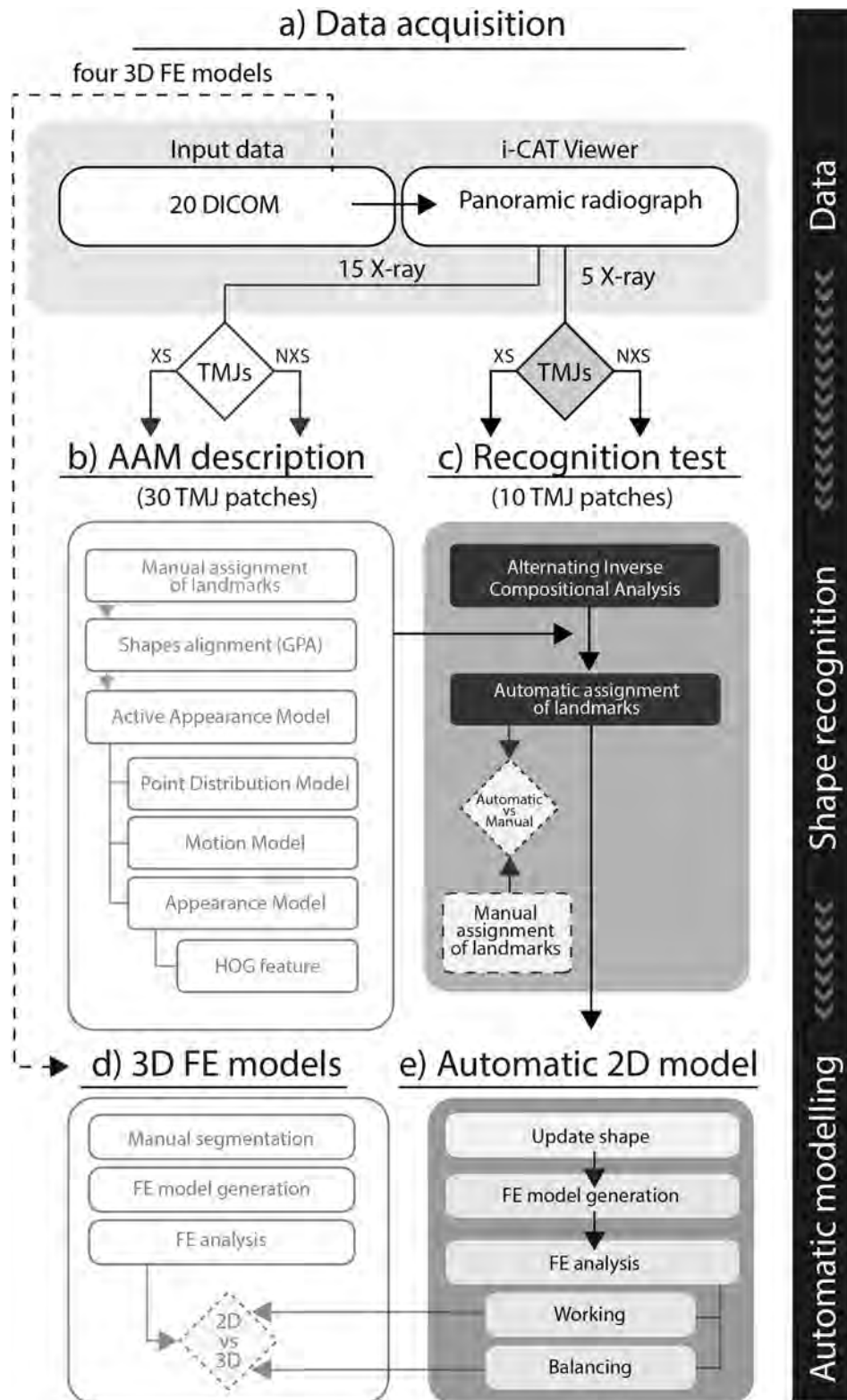
Figure 1. Flowchart showing the stages of the automated generation of FE models from panoramic radiographs: (a) data acquisition; (b) AAM description; (c) shape recognition in the area of the radiograph corresponding to the TMJ; (d) generation of the 3D FE model; and (e) automated 2D model generation. Diamonds with discontinuous lines represent the evaluation of image recognition according to manual segmentation and the differences between the 2D and 3D approaches (XS, cross bite side; NXS, non-cross bite side).

statistical deformable models (shape, motion, and appearance models), which are explained below:

Shape

A radiologist with expertise in TMD diagnosis located 21 landmarks (i points) grouped in 2 sets (16 and 5 points), corresponding to TMJ structures and the condyle, respectively (Figure 2a). Mathematically, each TMJ shape, s, was defined by the Cartesian coordinates of the i points as follows:

$$s = (x_1, y_1, x_2, y_2, \ldots \; x_i, y_i)^T \quad (1)$$

To align and normalise all shapes, generalised Procrustes analysis (GPA) (Figure 2b) was performed. Next, the statistical shape model or point distribution model (PDM) was computed by applying principal component analysis (PCA) to the dataset. Therefore, any shape (s) could be expressed as mean shape $\bar{s}$ plus a linear combination of n shape vectors, s_i, with the shape parameters p_i :

$$s = \bar{s} + \sum_{i=1}^{n} p_i s_i \quad (2)$$

Motion

The role of the motion model $\mathcal{W}(\mathbf{x}, p)$ was to extrapolate the position of all pixel positions $\mathbf{x}$ lying inside $\bar{s}$ from the template image to a deformable shape s generated by the combination of p parameters. The transformation was based on the relative position of i landmarks with respect to the sparse set of landmarks that defines the mean shape.

Appearance

The appearance model was generated by warping the original images onto the mean shape $\bar{s}$ using the previously defined motion model, $\mathcal{W}(\mathbf{x}, \; p)$. As described for the PDM, PCA was performed to define any appearance $A(\mathbf{x})$ of a set of pixels $\mathbf{x}$ as a mean appearance $\overline{A}(\mathbf{x})$ plus a linear combination of m appearance images, $A_i(\mathbf{x})$, with the appearance parameters c_i :

$$A(\mathbf{x}) = \overline{A}(\mathbf{x}) + \sum_{i=1}^{m} c_i A_i(\mathbf{x}) \quad (3)$$

HOG feature

After evaluation of the shape recognition results using different highly-descriptive, dense appearance features (Figure 3), the HOG feature was selected. The HOG feature clustered the gradient orientations into 9 bins (N_{bins}) for each cell of 8×8 pixels, and the cells were grouped in 2 blocks (N_{block}) of 2×2 cells for

normalisation of the gradients. Therefore, the HOG description dimension ($D = N_{bins}N_{block}{}^2$) consisted of 36 channels. The HOG feature transformed each 2D image (t) with size $H \times W$ into a multi-channel image using the feature extraction function $\mathcal{F} : \mathbb{R}^{H \times W} \rightarrow \mathbb{R}^{H \times W \times D}$.

Shape recognition algorithm

The shape recognition process was carried out using a minimisation process to fit the AAM to the input image (t). When the AAM is defined by highly-descriptive, dense appearance features, it is recommended to use the alternating inverse compositional (AIC) alignment algorithm (Antonakos et al. 2015). Like the IC algorithm, the aim of AIC algorithm is to find the corresponding N_A eigen texture in the subspace U_A ($U_A \in \mathbb{R}^{L_A \times \; N_A}$) of t, modifying parameters p and c in 2 separate minimisation problems, one for shape ($p \leftarrow p + \Delta p$) and another for appearance ($c \leftarrow c + \Delta c$). This iterative search algorithm can be mathematically expressed as minimising the following cost functions:

$$\begin{cases} \underset{\Delta p}{argmin} \left\| \mathcal{F}(t(\mathcal{W}(p))) - \mathcal{F}(\mathbf{a}_c(\mathcal{W}(\Delta p))) \right\|^2_{I - U_A U_A^T} \\ \underset{\Delta c}{argmin} \left\| \mathcal{F}(t(\mathcal{W}(p))) - \mathcal{F}(\mathbf{a}_{c + \Delta c}(\mathcal{W}(\Delta p))) \right\|^2 \end{cases}$$

$$(4)$$

where $\mathcal{F}(a_{c+\Delta c}(\mathcal{W}(\Delta p))) = \mathcal{F}(\bar{a}(\mathcal{W}(\Delta p))) + U_A \mathcal{F}(\mathcal{W}(\Delta p))(c + \Delta c)$ (Gross et al. 2005). Therefore, $\mathcal{F}(a_{c+\Delta c}(\mathcal{W}(\Delta p)))$ can be expressed by a first term of the mean appearance vector approximation and a second term of the linearised basis (Antonakos et al. 2015) of the U_A subspace of the AAM (where N_A and L_A are the eigen textures and the number of pixels inside $\bar{s}$, respectively). A fitting process of 100 iterations was executed for each of the 10 patches tested and was repeated 5 times to ensure model stabilisation. The fitting process was run on the same computer used for the AAM development and was completed after an average time of 43.89 s. Figure C1 of Appendix C in the supplementary material displays the landmarks paths throughout the recognition process. As described for the training set, an expert clinician identified landmarks for subsequent evaluation of recognition accuracy.
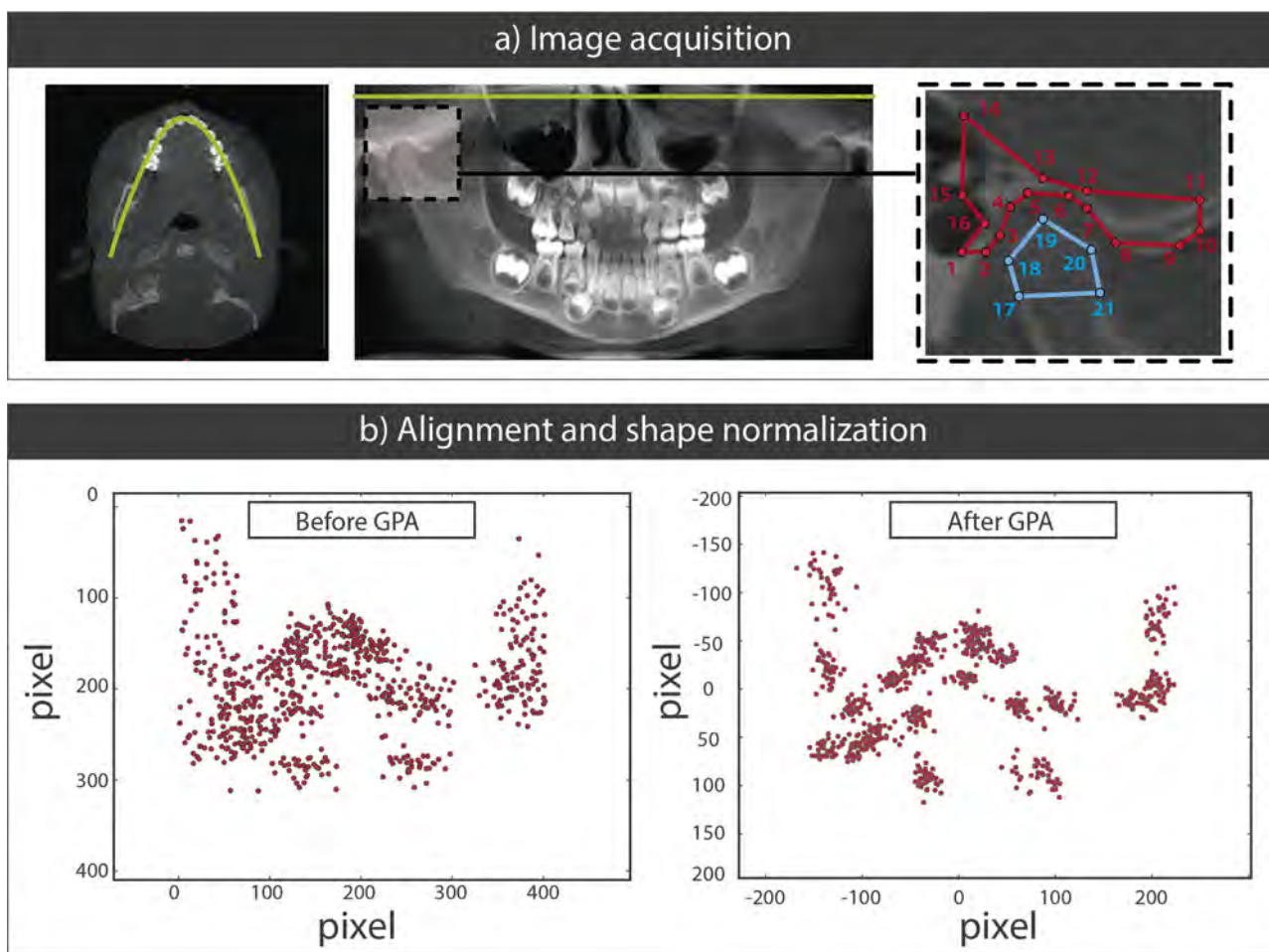
Figure 2. (a) From left to right: coronal slice of the CBCT scan, panoramic radiograph, and patch of the TMJ with landmarks. The unfold plane of the panoramic radiograph was defined as the midplane of the mandibular ramus thickness (green line). (b) Landmarks of the training dataset before (left) and after (right) shape normalisation by GPA.

Automated generation of a 2D finite element model

A script was written in Python to update the shape of a parametric CAD model in Abaqus commercial software (Abaqus 6.14, Simulia, Rhode Island, USA) using the recognised landmarks. This parametric model mimics the TMJ shape proposed by DeVocht and coworkers (DeVocht et al. 1996) using landmarks located in key morphological regions (Figure 4a) such as the articular eminence, the condylar head, and the TMJ disc space. The model consists of 6 parts (Figure 4a), some of which (TMJ disc and cartilage) were subdivided into 3 portions (anterior, central, and posterior) owing to the different mechanical behaviours of each region (Kim et al. 2003; Singh and Detamore 2008). For more details about the parametric model development, we recommend reading Appendix A of the supplementary material.

In setting the boundary conditions, the nodes of the anterior and posterior slices of the temporal bone were fixed and the contact between the TMJ disc and the cartilage was defined by a tangential friction coefficient of 0.015 (Tanaka et al. 2004) using a penalty contact formulation. The automatic modelling script ran 2 computational analyses of 2.5 s for each patient-specific shape to study chewing activity: in the first analysis the condyle compressed the TMJ disc with the mandibular fossa (working activity) and in the second the condyle moved along the articular eminence (balancing). The FE model was subjected to contractile forces produced by the connector's elements (CONN3D2-type element in Abaqus) that mimic the chewing muscles for both movements. The active, passive, and damping responses of each chewing muscle were defined following the procedure described in Appendix A of the supplementary material; whose parameters are likewise summarised in Table A2 of the same appendix.

In analysing the data produced, we assessed 16 mechanical variables (Table 1) and 3 geometrical variables, values of which were obtained from a script
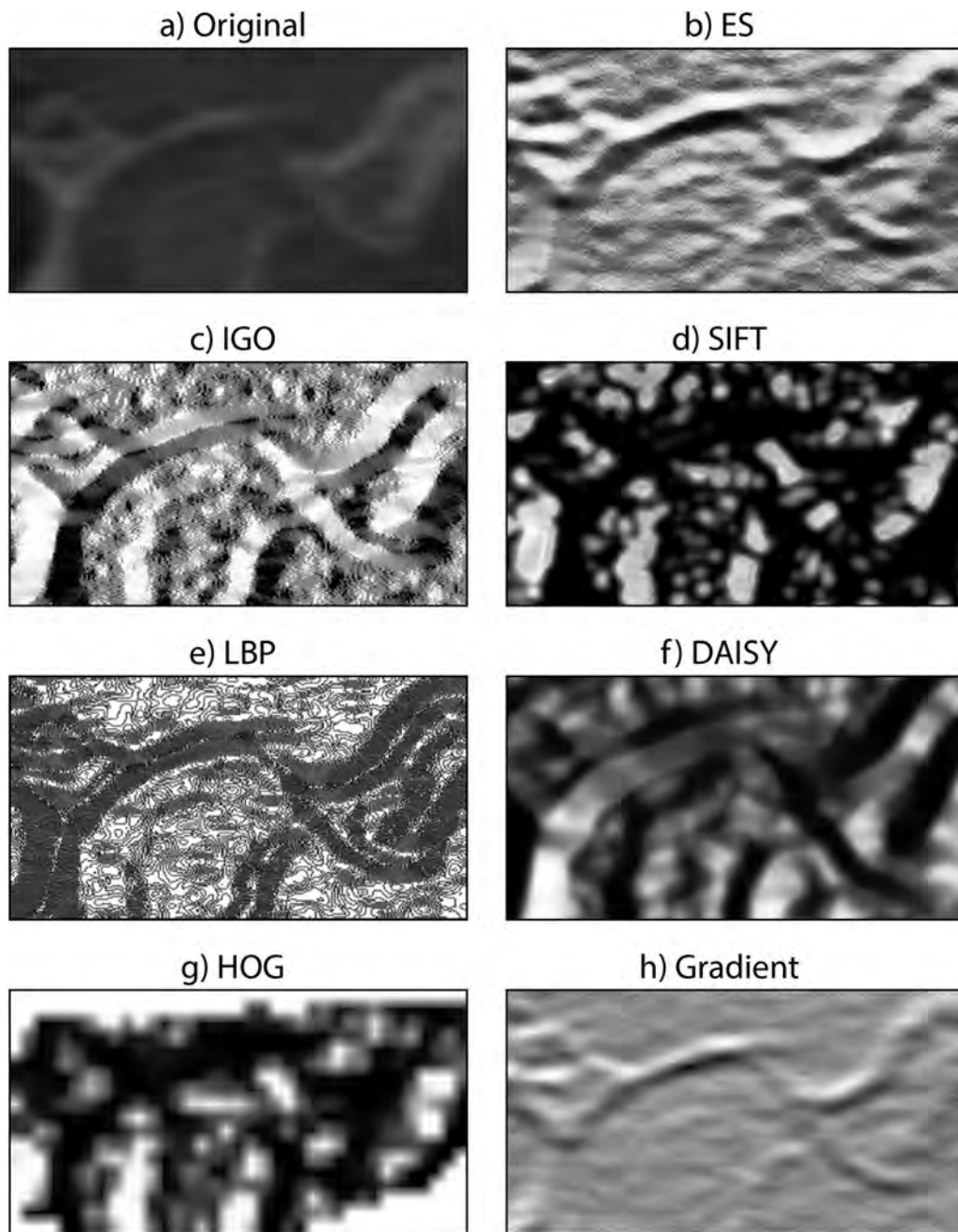
a) Original

b) ES

c) IGO

d) SIFT

e) LBP

f) DAISY

g) HOG

h) Gradient

Figure 3. (a) Patch of an original panoramic radiograph used as a template image to show the results of application of the following highly-descriptive, dense appearance features: (b) edge structures; (c) image gradient orientation kernel; (d) scale-invariant feature transform; (f) DAISY; (g) histograms of oriented gradients; (h) contour gradients.

written in Python. Based on the labelling of the cross bite side, the results were grouped in 2 sets depending on whether they were derived from the cross bite side (XS) or the non-cross bite side (NXS). A Mann-Whitney U-test was used to assess geometrical and mechanical differences between the TMJs on each side. The null hypothesis (i.e., no significant differences between the XS and NXS for a given variable) was accepted at p-values ≤ 0.05. Pearson's correlation coefficient, r, and its associated p-value were computed to assess relationships between the different variables for

both activities. The null hypothesis (a significant association between 2 variables) was accepted for p-values ≤ 0.05.

3D finite element models

Four CBCT datasets randomly chosen from the input data were also used to develop four complete 3D models for each patient. Although each dataset was previously segmented to identify the compact bony structures using a threshold level in Mimics
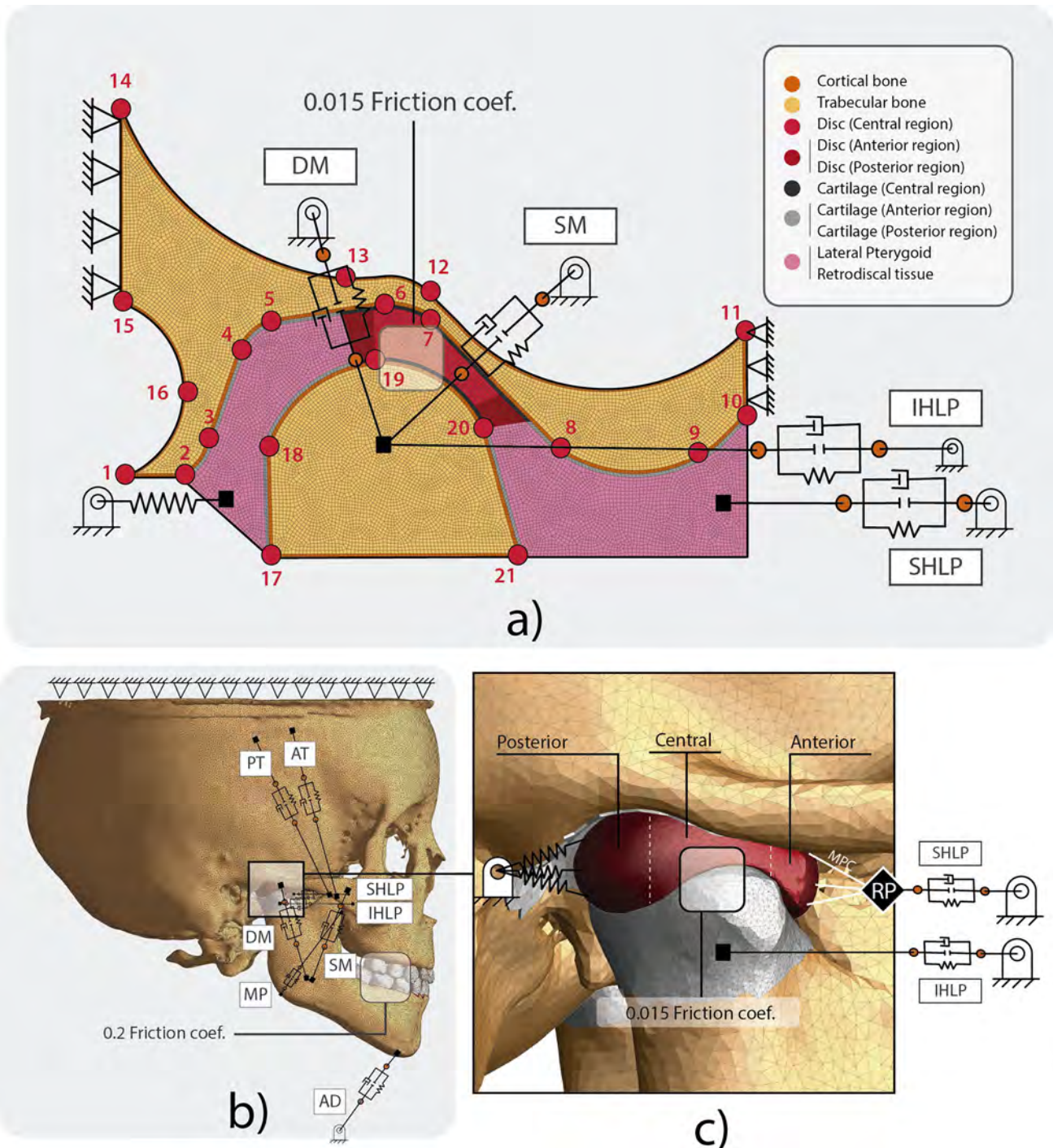
Figure 4. (a) 2D FE model of TMJ shape defined by the 21 landmarks (red points) and the applied boundary conditions. (b) 3D FE model generated manually from CBCT images and the boundary conditions applied. (c) Detail of the TMJ of the 3D FE model. (SM, superficial masseter; DM, deep masseter; SHLP, superior lateral pterygoid; IHLP, inferior lateral pterygoid; AT, anterior temporalis; PT, posterior temporalis; MP, medial pterygoid; AD, anterior depressor muscles; RP, reference point; MPC, multi-point constraint).

commercial software (Mimics, v.19.; Materialise, Leuven, Belgium), manual segmentation was required for cartilaginous and less dense bone regions. The mechanical properties, boundary conditions, muscle modelling, and disc friction coefficient were defined as in the 2D model (Figure 4b,c) and are also detailed in Appendix A of the supplemental material. Although 2 analyses were executed for each 2D model, only one was required in the 3D approach: while one condyle compresses the disc with the

Table 1. Geometrical and mechanical variables used in assessing differences between the XS (cross bite side) and NXS (non-cross bite side) groups during the two main TMJ movements (balancing and working). Data are presented as the mean, standard deviation (SD), and *p*-value (Mann-Whitney U-test). *$p < 0.05$.

Geometrical variables

Group	XS (n = 20)		NXS (n = 20)		
Variable	Mean	SD	Mean	SD	p value
Condyle width (mm)	9.06	1.31	7.96	1.22	0.0132*
Eminence inclination (rad)	0.70	0.07	0.53	0.07	<0.0001*
Temporal area (mm^2)	52.02	11.72	55.62	14.75	0.4135

Mechanical variables

Activity	Balancing					Working				
Group	XS (n = 20)		NXS (n = 20)			XS (n = 20)		NXS (n = 20)		
Variable	Mean	SD	Mean	SD	p value	Mean	SD	Mean	SD	p value
CTB -Min. Prin. Stress (MPa)	−6.35	3.17	−6.03	2.35	0.6849	−2.64	1.29	−2.02	1.08	0.1572
CTB -Max. Prin. Stress (MPa)	0.23	0.51	0.14	0.22	0.4247	0.17	0.27	0.04	0.05	0.0110*
CCB -Min. Prin. Stress (MPa)	−6.27	2.44	−6.44	2.08	0.8076	−2.80	1.15	−2.41	1.33	0.3791
CCB -Max. Prin. Stress (MPa)	0.16	0.18	0.17	0.25	0.4901	0.08	0.11	0.07	0.09	0.5517
TC (Ant) - Min. Prin. Stress (MPa)	−4.27	1.84	−4.14	1.53	0.5789	−0.05	0.05	−0.05	0.07	0.3575
TC (Cent) - Min. Prin. Stress (MPa)	−2.45	0.74	−2.38	0.77	0.7604	−2.18	1.04	−1.74	0.88	0.2118
TC (Post) - Min. Prin. Stress (MPa)	−0.05	0.02	−0.05	0.02	0.8603	−0.88	0.53	−0.68	0.44	0.2475
CC (Ant) - Min. Prin. Stress (MPa)	−0.98	0.76	−0.74	0.29	0.9138	−1.61	0.73	−1.37	0.83	0.3975
CC (Cent) - Min. Prin. Stress (MPa)	−4.43	1.43	−4.56	1.13	0.9396	−2.36	0.92	−1.97	1.00	0.2486
CC (Post) - Min. Prin. Stress (MPa)	0.00	0.00	−0.05	0.12	0.6948	−1.66	0.69	−1.30	0.71	0.0443*
TMJ disc (Ant) - Min. Prin. Stress (MPa)	−1.63	1.13	−1.68	1.55	0.8075	−0.61	0.39	−0.40	0.30	0.1363
TMJ disc (Cent) - Min. Prin. Stress (MPa)	−3.70	2.35	−3.46	2.02	0.6747	−1.16	0.20	−0.76	0.13	<0.0001*
TMJ disc (Post) - Min. Prin. Stress (MPa)	−0.05	0.02	−0.05	0.02	1.0000	−0.53	0.34	−0.35	0.25	0.0961
TMJ disc (Ant) - Contact Press. (MPa)	5.47	1.87	3.82	1.26	0.0080*	2.45	1.15	1.88	1.15	0.1293
TMJ disc (Cent) - Contact Press. (MPa)	4.88	2.35	4.23	1.81	0.4092	3.45	1.92	2.46	1.33	0.0979
TMJ disc (Post) - Contact Press. (MPa)	0.01	0.01	0.05	0.12	0.3646	2.92	1.72	2.12	1.12	0.2231

Note: CTB: Cortical portion of the temporal bone; CCB: Cortical portion of the condyle; TC: Temporal cartilage; CC: Condylar cartilage; Ant: Anterior region; Cent: Central region; Post: Posterior region; Min. Prin. Stress: Minimum Principal Stress; Max. Prin. Stress: Maximum Principal Stress; Contact. Press: Contact pressure
Condyle width: distance between landmarks 18 and 20.
Eminence inclination: slope of the line drawn between landmarks 7 and 8.
Temporal area: area enclosed between landmarks 7–12.

mandibular fossa (condyle of the working side), the other moves the articular eminence forward (condyle of the balancing side).

Results

Evaluation of the 2D approach

First, we compared the results of accurate 3D finite element models of the TMJ with those of the corresponding automatically generated 2D finite element model for patients S1 to S4. Within all stress components, the minimum principal stress in the solid phase of the TMJ discs was studied since compressive efforts were more significative than shear or tensile loads at both movements. Figure 5a,b show the minimum principal stress distribution whose mean and standard deviation values are summarised in Table B1 of the supplementary material. Comparison of both movements shows that balancing movement generated higher stresses in the disc than working movement (Figure 5c). This overloading resulted in greater absolute error between the two approaches for the balancing movement, as it can be

shown in Table B1 of the appendixes, supplementary material. Regardless, the results demonstrate good correspondence between the TMJ disc stresses determined using the two approaches, with a mean relative error of around 14%.

AAM and AIC alignment algorithm

The statistical models of TMJ shape and appearance are described by a series of principal variation components, which are formulated in Equations (2) and (3), respectively (Figure 6a). By sorting the values of the covariance matrix in descending order, the principal variation components are frequently renamed as principal variation modes, since the first principal components are the most representative modes of variation. The principal modes of the PDM characterised the anatomic shape variability of the TMJ, while the principal modes of the AAM represented the texture variations of the images. Therefore, an AAM with 5 principal modes accounted for over 70% of the total shape variability of the PDM. To explain 98% of variation in shape and appearance, 14 and 29 principal
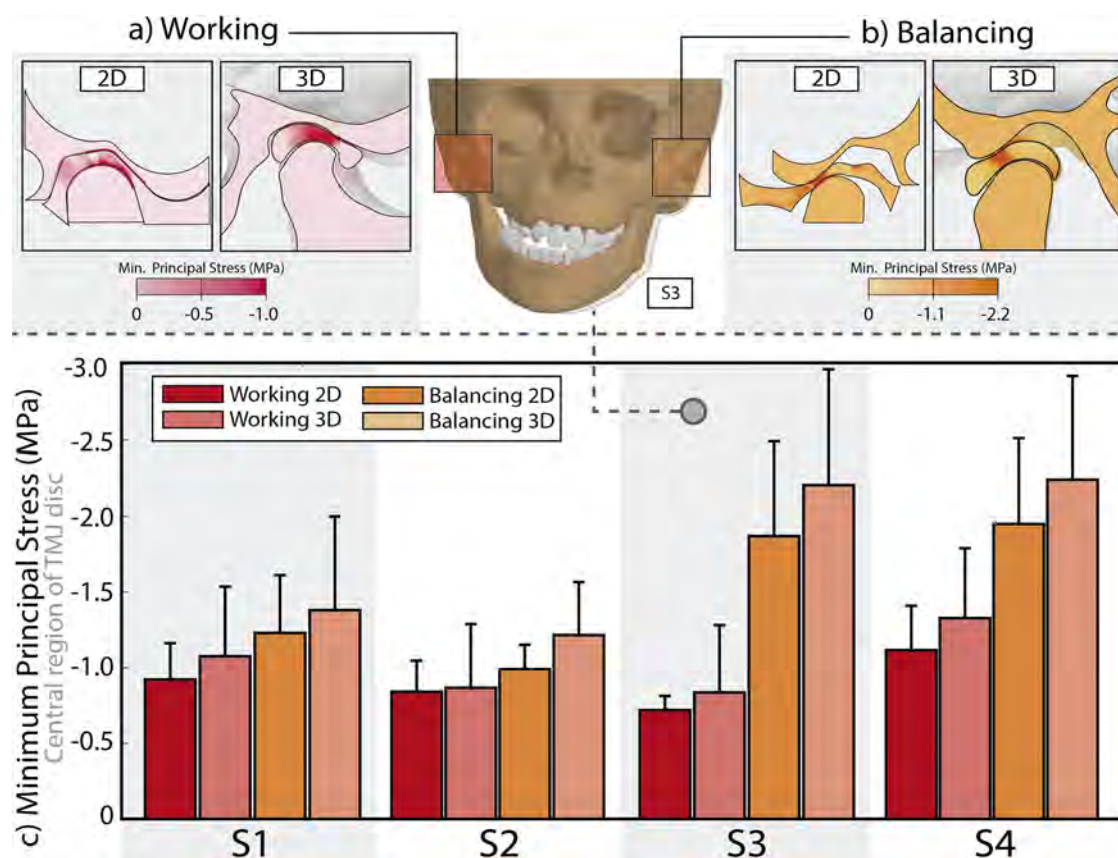
Figure 5. Minimum principal stress distribution in the TMJ during unilateral chewing on the (a) working side and (b) balancing side (left: 2D model results; right: 3D model results). (c) Mean and SD deviation of the minimum principal stresses in the central region of the TMJ disc of 4 subjects (S1–S4) during working (red and pink bars) and balancing (orange and yellow bars) movements as computed using 2D or 3D FE models. *Note: mean and standard deviation (SD) values are summarised in Table B1 in Appendix B, supplementary material.

modes were required, respectively. An animated representation of the principal variation modes of shape and appearance is shown in the supplementary material video. Although some studies (Sarkalkan, Weinans, et al. 2014; Hollenbeck et al. 2018) have reported different relationships between principal variation modes and anatomical references in other joints, in our study it was difficult to establish a relationship due to the high degree of variability in the sample's shape.

The AIC fitting algorithm modified the c_i and p_i parameters of the statistical AAM in order to minimise differences with respect to the input image. Figure C1 of the supplementary material shows the paths of the landmarks throughout the fitting procedure. First, the mean shape of the PDM was randomly located (Figure 6b). Next, the AIC algorithm gradually modified the AAM parameters, resulting in displacement of the landmarks (Figure 6c). The accuracy of the search was determined by calculating the point-to-point distance error for each landmark on the PDM, taking manually annotated landmarks as the true position (Figure 6c). In most cases, fitting stabilised by the 50th iteration, with fitting errors <10%. After the 50th of 100 iterations, the algorithm significantly altered landmark positions to ensure that the local optimum did not coincide with the global optimum. Fitting was quite stable for 75 iterations (fitting error <4%) and repetition of the algorithm revealed no significant differences for a single image (fitting error, 3.3–4.1%).

Mechanical analysis

Results were expressed as the mean value and the standard deviation (SD) for each of the different geometrical variables (condyle width, eminence inclination, and temporal area) and the mechanical variables separated by group (XS and NXS) and activity (working and balancing) (Table 1). Figure 7 shows the values for certain variables for which differences between the two sides were observed. From a morphological point of view, the mean width of the condyle and the inclination of the articular eminence were significantly greater in the XS group
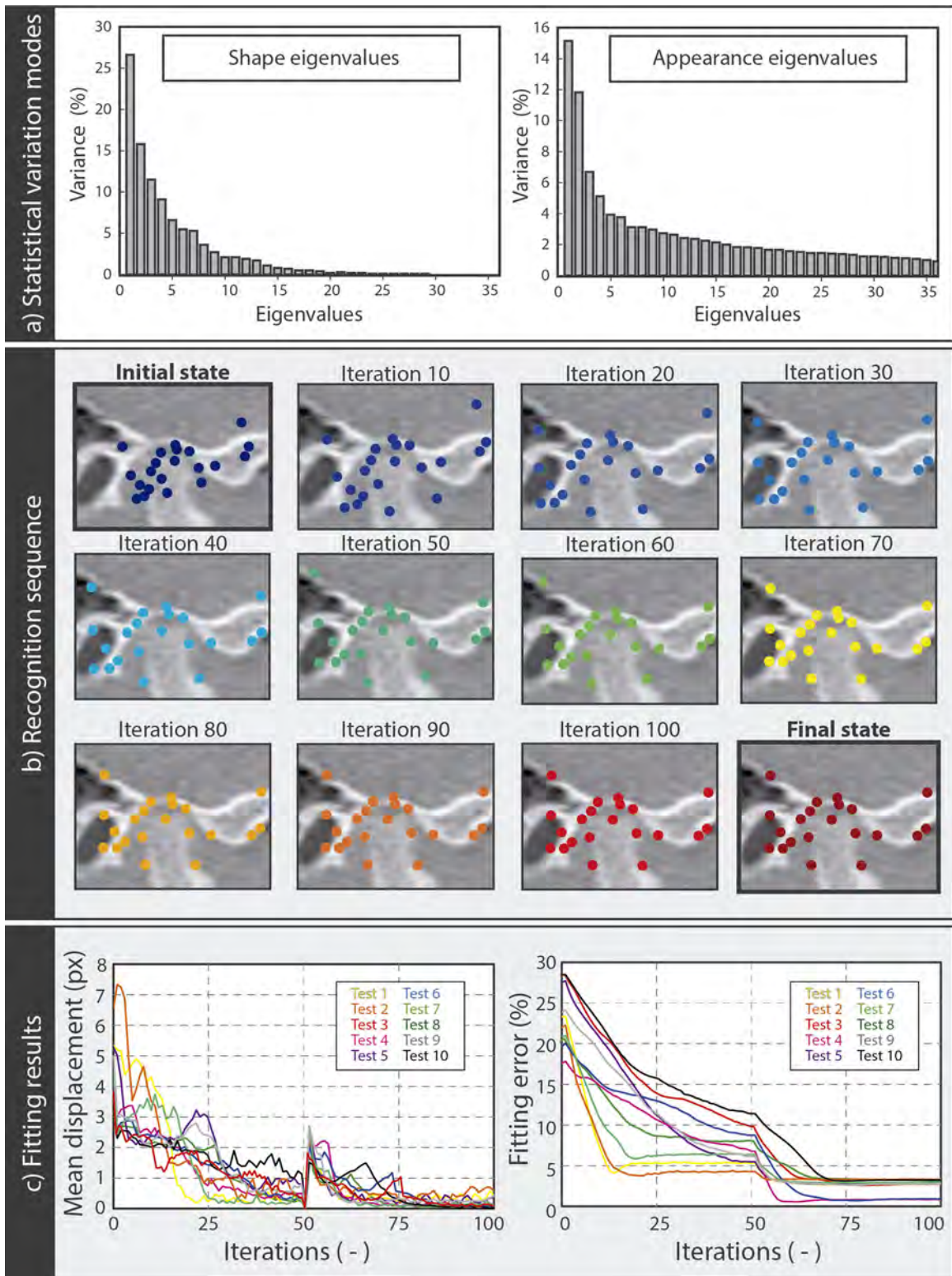
Figure 6. (a) Left, the percentage of shape variation described by the principal shape variation modes. Right, the percentage of appearance variation described by the principal appearance variation modes. (b) TMJ shape recognition sequence for 100 iterations. (c) Left, mean displacement in pixels (px) of the landmarks in each iteration. Right, shape model residual fitting errors (point-to-line, px) when refitting the shape model to the manually annotated contour. *Note: the landmark traces are shown in Figure C1 in Appendix C, supplementary material and in the supplementary video.
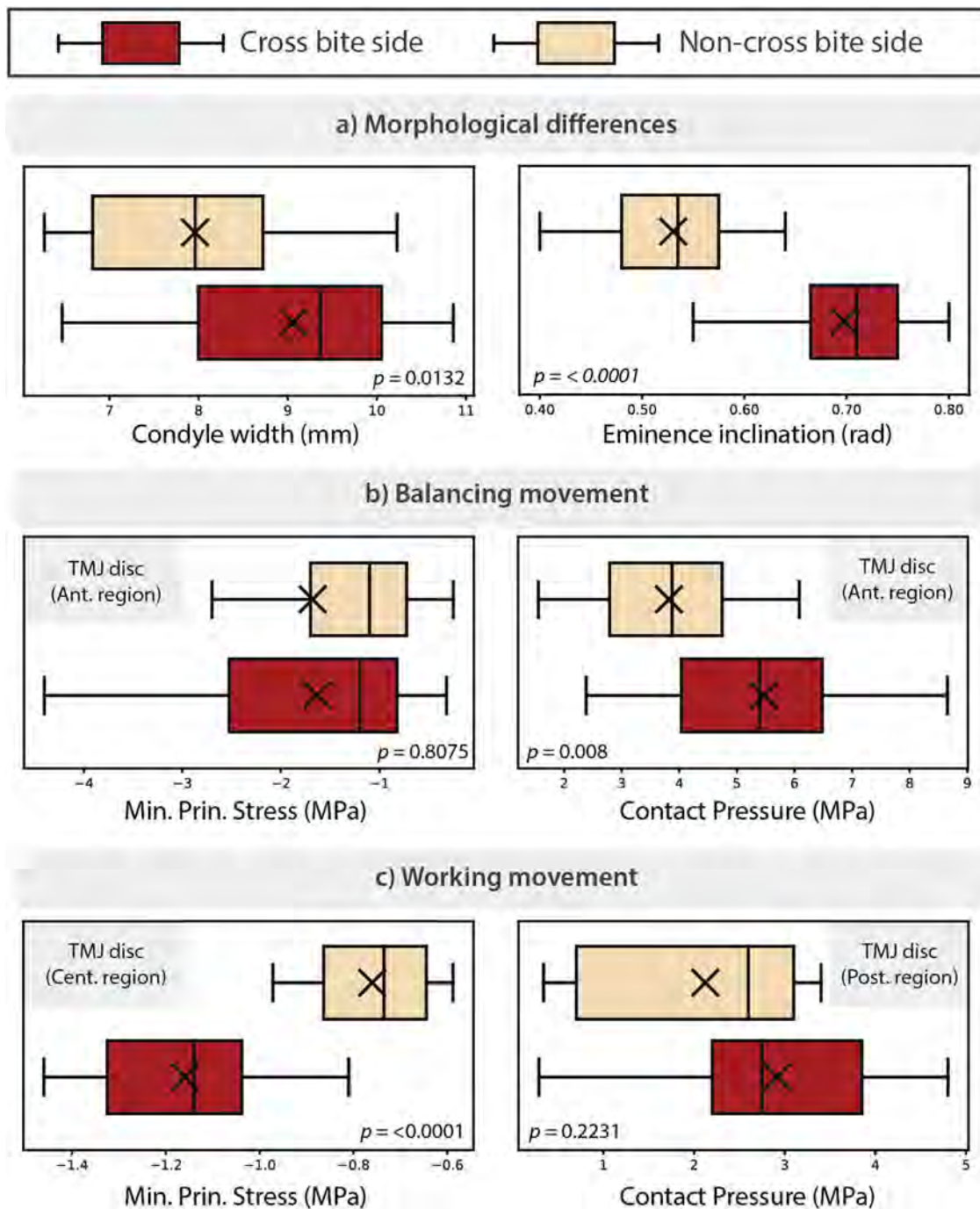
Figure 7. Boxplot for each group (red: cross bite side; yellow: non-cross bite side) indicating the median, 25th and 75th percentiles (box), and range of measurements (whiskers) for (a) geometrical variables and mechanical variables during (b) balancing and (c) working movement.

(9.06 ± 1.31 mm and 0.70 ± 0.07 rad) than in the NXS group (7.96 ± 1.22 mm and 0.53 ± 0.07 rad) (Figure 7a). Biomechanically, the contact pressure and the compressive stress (minimal principal stress) values in the anterior band of the XS discs were higher than those in the same region of the NXS discs (Figure 7b) during balancing movement. Likewise, during working movement, compressive stress values were significantly higher in the central region of the XS discs

than that of NXS discs, in which the posterior band was more loaded (Figure 7c). Pearson's correlation coefficients and associated p values for all the variables in both activities are summarised in tables of Appendix D, supplementary material, which are graphically displayed in Figure 8a of the manuscript. The results of the Mann-Whitney U-test and Pearson's correlation analysis revealed that articular eminence inclination differed significantly between
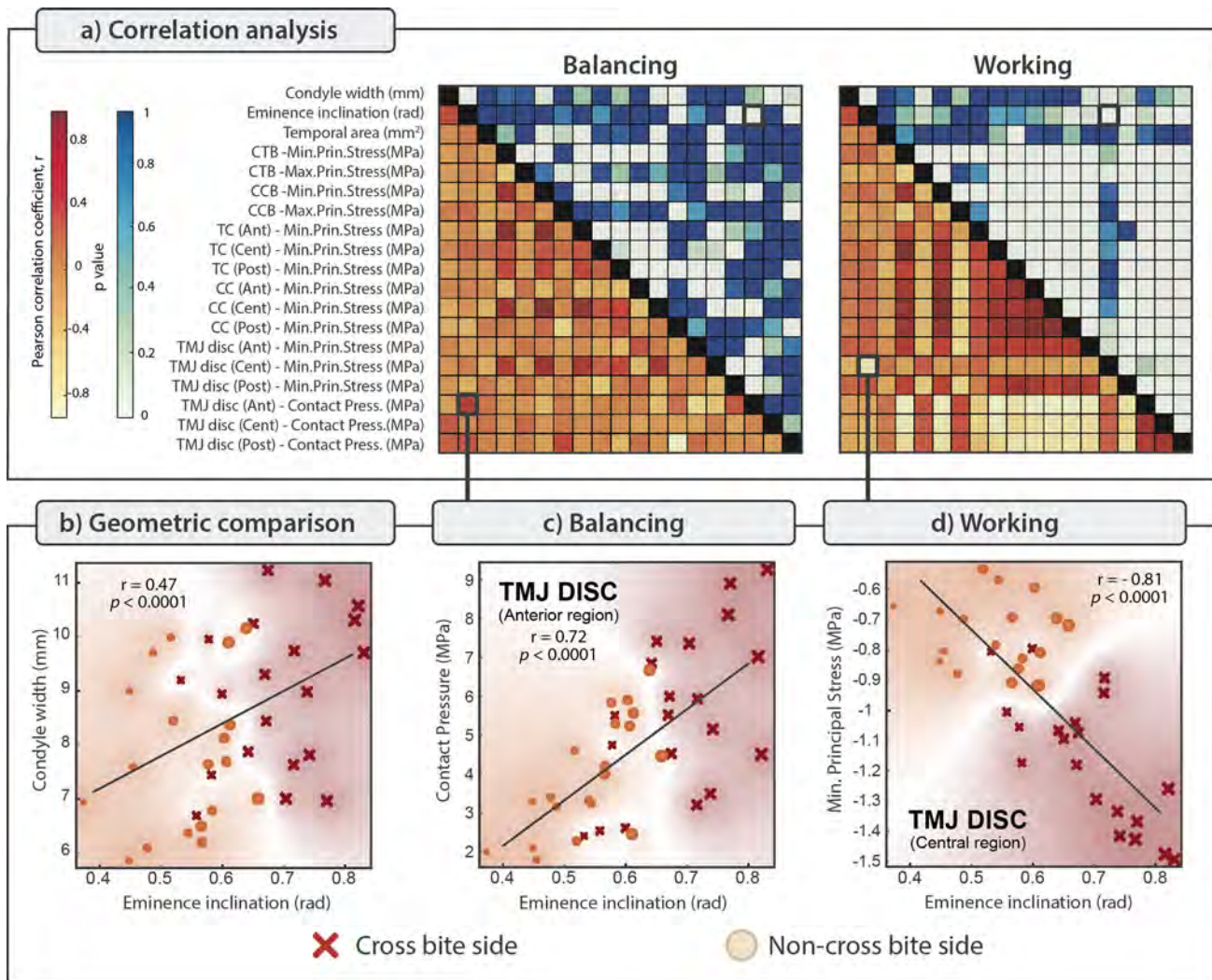
Figure 8. (a) Correlation matrix based on Pearson's correlation coefficient, r, and its associated probabilistic *p*-value. (b) Correlation between condyle width and inclination of the articular eminence. (c) Correlation between the contact pressure on the anterior region of the TMJ disc and the inclination of the articular eminence. (d) Correlation between the minimum principal stress of the central region of the TMJ disc and the inclination of the articular eminence. *Note: r and p values are summarised in Tables D1 and D2 in Appendix D, supplementary material.

groups (XS and NXS) and was significantly correlated with certain mechanical variables for both movements (Figure 8c,d). Therefore, we used this variable as an index of joint dysfunction in order to evaluate our results. Conversely, we observed no significant association (Figure 8b) between this variable and condyle width ($r = 0.47$) that would allow us to propose a geometric relationship.

Discussion

Early diagnosis of TMD would allow planning of paediatric treatments and help avoid complex or surgical procedures in adulthood. However, functional 3D evaluation of the TMJ is hindered by 2 key limitations. First, the generation of computational models of the TMJ of children requires a large amount of

manual work owing to the incomplete ossification of the bones, complicating patient-specific analyses. Second, 3D scans are not recommended for paediatric patients owing to the high radiation doses involved (De Felice et al. 2019). Therefore, diagnosis is often based on panoramic radiographs, which provide clinicians with limited data, and do not allow mechanical evaluation of the TMJ. We developed an automated tool for the generation of computational models of the TMJ through shape recognition using panoramic radiographs to facilitate the study, diagnosis, and treatment of TMDs during childhood. Specifically, we used this tool to study TMJ malformations due to UXB in paediatric patients.

The differences between 2D and 3D approaches were evaluated for 4 paediatric patients because 2D models assume a more simplified geometry than 3D

models generated using CT or CBCT images. The results (Figure 5c) revealed marked similarity between both approaches, with a mean relative error of 13%. Among other factors, this deviation may be due to the geometric simplification of the condylar head' shape or not considering the occlusion's role in the condyle's placement in the 2D model. For instance, during working movement, the occlusion's effect was not considered since the initial position of our models is already occluded and therefore, the condyles' upward movement is mainly induced by the masseter muscles' activities. At the same time, we consider that occlusal contacts on the balancing side hardly have any impact on the joint movement of this side, whose anterior movement is mainly guided by the temporal eminence and promoted by the action of the lateral pterygoid muscle. Biomechanically, the positive absolute error values (Appendix B, Table B1, supplementary material) suggest that during both working and balancing activity the solid phase of the TMJ disc is less loaded in the 2D than the 3D approach. The low load state of the solid phase in the 2D approach may be due to the differing degrees of freedoms between the two models. In the 3D approach, the fluid can flow in all directions, while in the 2D approach the fluid cannot drain perpendicular to the plane of the 2D model. This may explain the less compressible response of the TMJ disc in the 2D simulations (Figure 5c), and the resulting decrease in the stress supported by the solid phase.

The results shown in Figure 6 demonstrate the accuracy of the shape recognition algorithm and validate the AAM and AIC fitting algorithm for the TMJ shape recognition. The 10 fitting tests performed to validate the algorithm produced a fitting error (<4%) that was slightly greater than the intra-observer variability recorded during manual segmentation. Moreover, the algorithm showed good repeatability for each image, producing results consistent with those of other studies studies (Roberts et al. 2010; Roberts et al. 2012; Sarkalkan, Waarsing, et al. 2014) in which a similar 2D recognition technique was applied to other joints. It should be noted that automated segmentation in paediatric patients is more difficult owing to the incomplete ossification of bones in these individuals. However, the use of HOG features, a novel aspect of this study, improves the convergence of the fitting process.

The manually defined landmarks and those automatically detected by the AIC alignment algorithm were used to adapt the dimensions of our parametric FE model. We observed a significant difference

($p < 0.05$) between the XS and NXS groups in the slope of the articular eminence, which was more pronounced in the former group (Figure 7a). Our findings are consistent with those of other researchers (Pirttiniemi et al. 1990; Wohlberg et al. 2012) who empirically detected an increase in the slope of the articular eminence in the XS group. We also found that the condyle width was significantly greater in the XS than the NXS group, in agreement with the findings of Veli and coworkers (Veli et al. 2011). However, in contrast to the findings of previous empirical studies (Prakash and Durgesh 2011; Planas 2013; Tsanidis et al. 2016), we observed no significant relationship between eminence slope and condyle head width, likely due to the incomplete development of the condyloid process in our patients (Karlo et al. 2010).

From a biomechanical point of view, the compressive stresses were more uniformly distributed throughout the disc during working movement than balancing movement, mainly due to the key role of the intra-articular fluid component. During balancing movement contact pressures were higher in the anterior and central regions of the disc in the XS and NXS groups, respectively. Analysis of the correlation between morpho-functional variables revealed a negative regression between the compressive stress magnitude in the central region of the disc and the condylar head width (Figure 8a). This finding may numerically reflect the increase in condylar head volume caused by bone mechanical adaptation. During balancing movement, we observed a positive association between articular eminence slope and compressive stress in the anterior band of the disc. This observation may confirm a previously proposed hypothesis (Widman 1988; Pirttiniemi et al. 1990; Mimura and Deguchi 1994; Wohlberg et al. 2012) that speculated about an association between a steeper articular eminence slope and a greater mechanical stimulus on the XS. Conversely, the less steep slope of the articular eminence on the NXS may be a consequence of the shear stimulus that occurs on this side (the usual balancing side). Our findings thus reject the null hypothesis that TMJ malformations are unrelated to TMJ dysfunction.

Limitations

Despite the important implications of this study, several limitations should be noted. First, the simplified 2D FE model did not mirror the mechanical environment as accurately as 3D approaches where, for

instance, the key role of occlusal contacts in mandible positioning is considered. Therefore, our results must be interpreted with caution and only qualitative differences between XS and NXS should be considered. Furthermore, soft tissue shape and mechanical behaviour may differ significantly between subjects. Finally, these findings apply specifically to 6–12-year-old patients with UXB and cannot be extrapolated to all TMD patients.

Conclusion

We have developed a computational tool for automated generation of 2D FE models of the TMJ based on panoramic radiographs and describe its use to study the shape-function relationship of the TMJ in paediatric patients with UXB. Within the limitations of this study, the following conclusions can be drawn:

- Statistical deformable models are powerful tools for the mechanical study of the TMJ, allowing tailoring of clinical computational studies to the specific shape of each patient.
- Although 2D models revealed several qualitative differences between the TMJs of opposing jaws, these models cannot be recommended for precise measurement of mechanical variables (range of error, 3–19%).
- The anterior disc band of the cross bite side was more loaded than that of the non-cross bite side. This may result in functional limitation of the joint on the crossbite side.
- There is a significant relationship between the width of the condyle and its functional activity on the usual working side (i.e. the cross bite side).
- The articular eminence slope of the cross bite side is greater than that of the non-cross bite side and is significantly associated with a decrease in balancing activity.

In summary, the proposed methodology was successfully applied in orthopaedics, providing helpful results to understand the influence of TMJ development in biomechanical function and further TMDs. Nonetheless, this methodology could be also applied in many other areas, such as anatomy and medicine, to investigate the effect of bone deformities in the mechanical environment or help in the diagnosis and treatment of several pathologies. For all these applications, further research effort will be required to increase the number of training examples, improve the accuracy of new statistical shape and appearance models, and allow patient-specific approaches.

References

Alabort-I-Medina J, Antonakos E, Booth J, Snape P, Zafeiriou S. 2014. Menp. In: Proc ACM Int Conf Multimed - MM '14. New York (NY): ACM Press; p. 679–682.

Antonakos E, Alabort-I-Medina J, Tzimiropoulos G, Zafeiriou SP. 2015. Feature-based Lucas–Kanade and active appearance models. IEEE Trans Image Process. 24(9):2617–2632.

Baker S, Matthews I. 2004. Lucas-Kanade 20 years on: a unifying framework. Int J Comput Vis. 56(3):221–255.

Bakke M. 2006. Bite force and occlusion. Semin Orthod. 12(2):120–126.

Bredbenner TL, Eliason TD, Potter RS, Mason RL, Havill LM, Nicolella DP. 2010. Statistical shape modeling describes variation in tibia and femur surface geometry between control and Incidence groups from the Osteoarthritis Initiative database. J Biomech. 43(9): 1780–1786.

Chan HJ, Woods M, Stella D. 2008. Mandibular muscle morphology in children with different vertical facial patterns: a 3-dimensional computed tomography study. Am J Orthod Dentofac Orthop. 133:1–13.

Cootes TF, Taylor CJ. 2001. On representing edge structure for model matching. In: Proc 2001 IEEE Comput Soc Conf Comput Vis Pattern Recognition CVPR 2001. Vol. 1. Kauai (HI): IEEE Comput. Soc; p. I-1114–I-1119.

Cootes TF, Taylor CJ, Cooper DH, Graham J. 1995. Active shape models-their training and application. Comput Vis Image Underst. 61(1):38–59.

Dalal N, Triggs B. 2005. Histograms of oriented gradients for human detection. In: 2005 IEEE Comput Soc Conf Comput Vis Pattern Recognit. Vol. 1. San Diego (CA): IEEE; p. 886–893.

DeVocht JW, Goel VK, Zeitler DL, Lew D. 1996. A study of the control of disc movement within the temporomandibular joint using the finite element technique. J Oral Maxillofac Surg. 54(12):1431–1437.

Dimitroulis G. 2018. Management of temporomandibular joint disorders: a surgeon's perspective. Aust Dent J. 63: S79–S90.

Dornaika F, Ahlberg J. 2006. Fitting 3D face models for tracking and active appearance model training. Image Vis Comput. 24(9):1010–1024.

De Felice F, Di Carlo G, Saccucci M, Tombolini V, Polimeni A. 2019. Dental cone beam computed tomography in children: clinical effectiveness and cancer risk due to radiation exposure. Oncology. 96(4):173–178.

Gross R, Matthews I, Baker S. 2005. Generic vs. person specific active appearance models. Image Vis Comput. 23(12):1080–1093.

Hollenbeck JFM, Cain CM, Fattor JA, Rullkoetter PJ, Laz PJ. 2018. Statistical shape modeling characterizes three-dimensional shape and alignment variability in the lumbar spine. J Biomech. 69:146–155.

Illipronti-Filho E, Fantini S. d, Chilvarquer I. 2015. Evaluation of mandibular condyles in children with unilateral posterior crossbite. Braz Oral Res. 29(1):1–7.

Karlo CA, Stolzmann P, Habernig S, Müller L, Saurenmann T, Kellenberger CJ. 2010. Size, shape and age-related changes of the mandibular condyle during childhood. Eur Radiol. 20(10):2512–2517.

Kim K-W, Wong ME, Helfrick JF, Thomas JB, Athanasiou KA. 2003. Biomechanical tissue characterization of the superior joint space of the porcine temporomandibular joint. Ann Biomed Eng. 31(8):924–930.

Lee TS. 1996. Image representation using 2D Gabor wavelets. IEEE Trans Pattern Anal Mach Intell. 18:959–971.

Lowe DG. 1999. Object recognition from local scale-invariant features. In: Proc Seventh IEEE Int Conf Comput Vis. Vol. 2. Kerkyra: IEEE; p. 1150–1157.

Mimura H, Deguchi T. 1994. Relationship between sagittal condylar path and the degree of mandibular asymmetry in unilateral cross-bite patients. CRANIO®. 12(3):161–166.

Ojala T, Pietikäinen M, Mäenpää T. 2001. A generalized local binary pattern operator for multiresolution gray scale and rotation invariant texture classification. In: Int Conf Adv Pattern Recognit. [place unknown]: Springer; p. 399–408.

Ortún-Terrazas J, Fagan MJ, Cegoñino J, Illipronti-Filho E, Pérez del Palomar A. 2020. Towards an early 3D-diagnosis of craniofacial asymmetry by computing the accurate midplane. a PCA-based method. Comput Methods Programs Biomed. 191:105397.

Palla S, Gallo L, Gossi D. 2003. Dynamic stereometry of the temporomandibular joint. Orthod Craniofac Res. 6(s1):37–47.

Pirttiniemi P, Kantomaa T, Lahtela P. 1990. Relationship between craniofacial and condyle path asymmetry in unilateral cross-bite patients. Eur J Orthod. 12(4):408–413.

Planas P. 2013. Neuro-occlusal rehabilitation: NOR. 2nd ed. Barcelona: Amolca.

Prakash P, Durgesh BH. 2011. Anterior crossbite correction in early mixed dentition period using Catlan's appliance: a case report. ISRN Dent. 2011:1–5.

Roberts MG, Graham J, Devlin H. 2010. Improving the detection of osteoporosis from dental radiographs using active appearance models. In: 2010 IEEE Int Symp Biomed Imaging from Nano to Macro. Rotterdam: IEEE; p. 440–443.

Roberts MG, Oh T, Pacheco EMB, Mohankumar R, Cootes TF, Adams JE. 2012. Semi-automatic determination of detailed vertebral shape from lumbar radiographs using active appearance models. Osteoporos Int. 23(2):655–664.

Sarkalkan N, Waarsing JH, Bos PK, Weinans H, Zadpoor AA. 2014. Statistical shape and appearance models for fast and automated estimation of proximal femur fracture load using 2D finite element models. J Biomech. 47(12):3107–3114.

Sarkalkan N, Weinans H, Zadpoor AA. 2014. Statistical shape and appearance models of bones. Bone. 60:129–140.

Shan ZY, Parra C, Ji Q, Jain J, Reddick WE. 2006. A knowledge-guided active model method of cortical structure segmentation on pediatric MR images. J Magn Reson Imaging. 24(4):779–789.

Singh M, Detamore MS. 2008. Tensile properties of the mandibular condylar cartilage. J Biomech Eng. 130(1):011009. doi:10.1115/1.2838062.

Tanaka E, Kawai N, Tanaka M, Todoh M, van Eijden T, Hanaoka K, Dalla-Bona DA, Takata T, Tanne K. 2004. The frictional coefficient of the temporomandibular joint and its dependency on the magnitude and duration of joint loading. J Dent Res. 83(5):404–407.

Thiesen G, Gribel BF, Freitas M. 2015. Facial asymmetry: a current review. Dental Press J Orthod. 20(6):110–125.

Tsanidis N, Antonarakis GS, Kiliaridis S. 2016. Functional changes after early treatment of unilateral posterior cross-bite associated with mandibular shift: a systematic review. J Oral Rehabil. 43(1):59–68.

Tzimiropoulos G, Zafeiriou S, Pantic M. 2012. Subspace learning from image gradient orientations. IEEE Trans Pattern Anal Mach Intell. 34(12):2454–2466.

Veli I, Uysal T, Ozer T, Ucar FI, Eruz M. 2011. Mandibular asymmetry in unilateral and bilateral posterior crossbite patients using cone-beam computed tomography. Angle Orthod. 81(6):966–974.

Widman DJ. 1988. Functional and morphologic considerations of the articular eminence. Angle Orthod. 58:221–236.

Wohlberg V, Schwahn C, Gesch D, Meyer G, Kocher T, Bernhardt O. 2012. The association between anterior crossbite, deep bite and temporomandibular joint morphology validated by magnetic resonance imaging in an adult non-patient group. Ann Anat - Anat Anzeiger. 194(4):339–344.